RESEARCH/REVIEW ARTICLE

Reflection and transmission of irradiance by snow and sea ice in the central Arctic Ocean in summer 2010

Ruibo Lei,[1,2] Zhanhai Zhang,[1] Ilkka Matero,[3] Bin Cheng,[4] Qun Li[1] & Wenfeng Huang[5]

[1] Polar Oceanography Division, Polar Research Institute of China, 451 Jinqiao Road, Pudong, 200136 Shanghai, China
[2] State Key Laboratory of Marine Geology, Tongji University, 1239 Siping Road, 200092 Shanghai, China
[3] Department of Physics, University of Helsinki, PO Box 48, FI-00014 Helsinki, Finland
[4] Marine Department, Finnish Meteorological Institute, PO Box 503, FI-00101 Helsinki, Finland
[5] State Key Laboratory of Coastal and Offshore Engineering, Dalian University of Technology, 2 Linggong Road, 116024 Dalian, China

Keywords
Sea ice; snow; solar irradiance; reflection; transmission; Arctic.

Correspondence
Ruibo Lei, Polar Oceanography Division, Polar Research Institute of China, 451 Jinqiao Road, Pudong, 200136 Shanghai, China.
E-mail: leiruibo@pric.gov.cn

Abstract

Reflection and transmission of irradiance by the combined snow and sea ice layer were measured at an ice camp (ca. 10 days) and several short-term stations (ca. 2 h) established in the western sector of the Arctic Ocean above 80°N during the 2010 summer. These measurements were made with an intention to quantify the apparent optical properties of snow and sea ice, and to evaluate their roles in the mass balance of snow-covered sea ice in the High Arctic. The integrated 350–920 nm albedo ranged from 0.54 to 0.88, and was primarily dependent on the geophysical properties of snow, but not those of sea ice. This implies that all snow cover was still optically thick, even though snow melting had commenced at all measurement sites. For sea ice about 1.66 m thick and covered by 2.5–8.5 cm of snow at the ice camp, the integrated 350–920 nm transmittance ranged from 0.017 to 0.065. Rapid snow melting resulting from an event of slight drizzle doubled the available solar irradiance under the ice (from ca. 3.6 to 7.2 $W \cdot m^{-2}$), which further accelerated ice-bottom decay. During the measurement at the camp, the temporally averaged incident solar irradiance at 320–950 nm was 110.6 ± 33.6 $W \cdot m^{-2}$, $29.2 \pm 2.9\%$ of which was absorbed by snow and sea ice and utilized to melt snow and sea ice. The melting of snow and sea ice had a distinctly greater effect on the spectral reflection and transmission for the near-infrared spectrum than for the ultraviolet and visible spectra.

Sea ice is a crucial component of the global climate system, and has long been considered as an effective climatologic indicator owing to its sensitivity to climate change. There has been increasing evidence of a dramatic reduction in the Arctic sea ice during the past few decades. The annual Arctic sea-ice extent has decreased by about 2.2–3.0% per decade from 1979 to 2007 (Comiso et al. 2008). Combined analysis using submarine and ICESat data shows that the average Arctic sea-ice thickness at the end of the melt season for the years 2003–08 has decreased by 1.6 m relative to that in the years 1958–1976 (Kwok & Rothrock 2009).

The ice-albedo feedback is a key link between the sea-ice mass balance and climate. Snow and sea ice act as filters of solar radiation, lowering its level and modifying its spectrum, and consequently keeping the Arctic Ocean cool and moderating global climate. Reduction of Arctic snow and sea ice leads to more radiation being transmitted into the upper ocean (Perovich et al. 2007; Inoue et al. 2008), which accelerates further melting of sea ice. During summer, solar radiation is a major energy source for the internal melting of sea ice. To understand the role of solar radiation in quantitative detail, considerable efforts have been devoted to understanding the temporal development of the albedos of sea ices with various surface types (Perovich et al. 2002). Comparing with surface albedo measurements, there are relatively few field investigations of the transmission and absorption of

Citation: *Polar Research* 2012, *31*, 17325, DOI: 10.3402/polar.v31i0.17325

solar irradiance by Arctic sea ice, owing to the difficulty of setting up optical sensors within/under sea ice. Most previous field studies on irradiance transmission through sea ice were limited to spot measurements (Ehn et al. 2008; Light et al. 2008). The technology for in situ measurements of snow and sea-ice mass balance has been fully developed (Richter-Menge et al. 2006; Lei et al. 2009). Even over one floe, the snow and sea-ice geophysical properties have great spatial variability (Sturm et al. 2002; Perovich et al. 2003). It is therefore difficult to match the results from continuous observations of the snow and sea-ice mass balance and the results from discrete observations of the vertical partitioning of solar radiation. Nicolaus, Hudson et al. (2010) developed a sophisticated platform to make synchronous, autonomous, continuous and high-temporal-resolution measurements of spectral albedo and transmittance for sea ice, which allows us to collect more high quality data for the process-related studies. However, this kind of field study is still in its preliminary stage and data are still not widely available, even though they are required to thoroughly understand the response of snow and sea ice over the Arctic Ocean to global climate change.

A connection among the geophysical, biological and optical properties of snow and sea ice has long been recognized (e.g., Grenfell & Maykut 1977; Mundy et al. 2007). Photosynthetically active radiation (PAR), with a wavelength band from 400 to 700 nm, is of special interest in biological investigations. Since there is a close relation between biological mass/category and snow/sea-ice apparent optical properties at particular wavelengths (Perovich et al. 1993; Mundy et al. 2007; Ehn et al. 2008), it is necessary to characterize snow/sea-ice apparent optical properties with a high spectral resolution, especially in the PAR region. The ground-optical measurement of sea ice, especially the spectral albedo measurement, is also important for the interpretation of products derived from remote sensing at visible and near-infrared wavelengths. Instruments used in such remote sensing include the satellite-borne Moderate Resolution Imaging Spectroradiometer and Advanced Very High Resolution Radiometer (Pavelsky & Smith 2004; Tschudi et al. 2008).

Here, we present a continuous in situ measurement lasting about 10 days and several spot measurements for the spectral albedo and transmittance and the mass balance of snow and sea ice in the High Arctic during the Chinese National Arctic Research Expedition carried out in the summer of 2010 (CHINARE-2010). The measurement employs a platform similar to that presented by Nicolaus, Hudson et al. (2010). However, our platform is more adaptive for temporal application, and thus effectively avoids the influence of the borehole on the irradiance transmission. The objectives of this study were to (1) quantify solar radiation vertical partitioning in the atmosphere, snow, sea ice and upper ocean in the High Arctic, where available data are relative sparse, (2) characterize the spectral albedo and transmittance of snow-covered sea ice and their wavelength dependences, and (3) investigate the interaction between the snow/sea-ice mass balance and solar radiation vertical partitioning.

Methods

Fieldwork

The State Oceanic Administration of China has organized a few CHINARE cruises in the Western sector of the Arctic Ocean since 1999 using the Chinese ice breaker RV *Xuelong*. All cruises were in summer. One of the motivations for these expeditions is to better understand how sea ice in the Arctic is responding to global climate change. Compared with previous cruises, the R/V *Xuelong* sailed much further north during the CHINARE-2010 cruise. Six short-term ice stations (ca. 2 h) and one long-term ice camp (ca. 10 days) were set up in the High Arctic to investigate the reflection or/and transmission of irradiance by snow and sea ice (Fig. 1).

Short-term observations. At short-term stations, spectral reflectance measurements were performed with two TriOS (Oldenburg, Germany) RAMSES ACC-2 VIS hyper-spectral radiometers (hereafter referred to as RAMSES sensors). The RAMSES sensor is equipped with a cosine collector to detect irradiance ranging from 320 to 950 nm, covering the primary spectrum that can be transmitted through a combined snow and sea-ice layer (Winther et al. 2004). Its viewing field is a full hemisphere. Light is channelled by an optical fibre, separated into its constituent wavelengths by a holographic grating, and detected by a 256-channel photodiode array. The sensor therefore has average spectral resolution of 3.3 nm. The sensitivity is as fine as $4{\cdot}10^{-5}$ W m^{-2} nm^{-1}, and spectral accuracy is 0.3 nm. Each sensor includes an electronic unit controlling the measurements. The data were stored in a TriOS DSP data logger. Two sensors were set up using two tripods with a connecting horizontal bar with a length of 4 m (Fig. 2). The sensors were mounted at the centre of the bar, with one looking upward and the other one looking downward vertically, to monitor incident and reflected

Citation: *Polar Research* 2012, *31*, 17325, DOI: 10.3402/polar.v31i0.17325

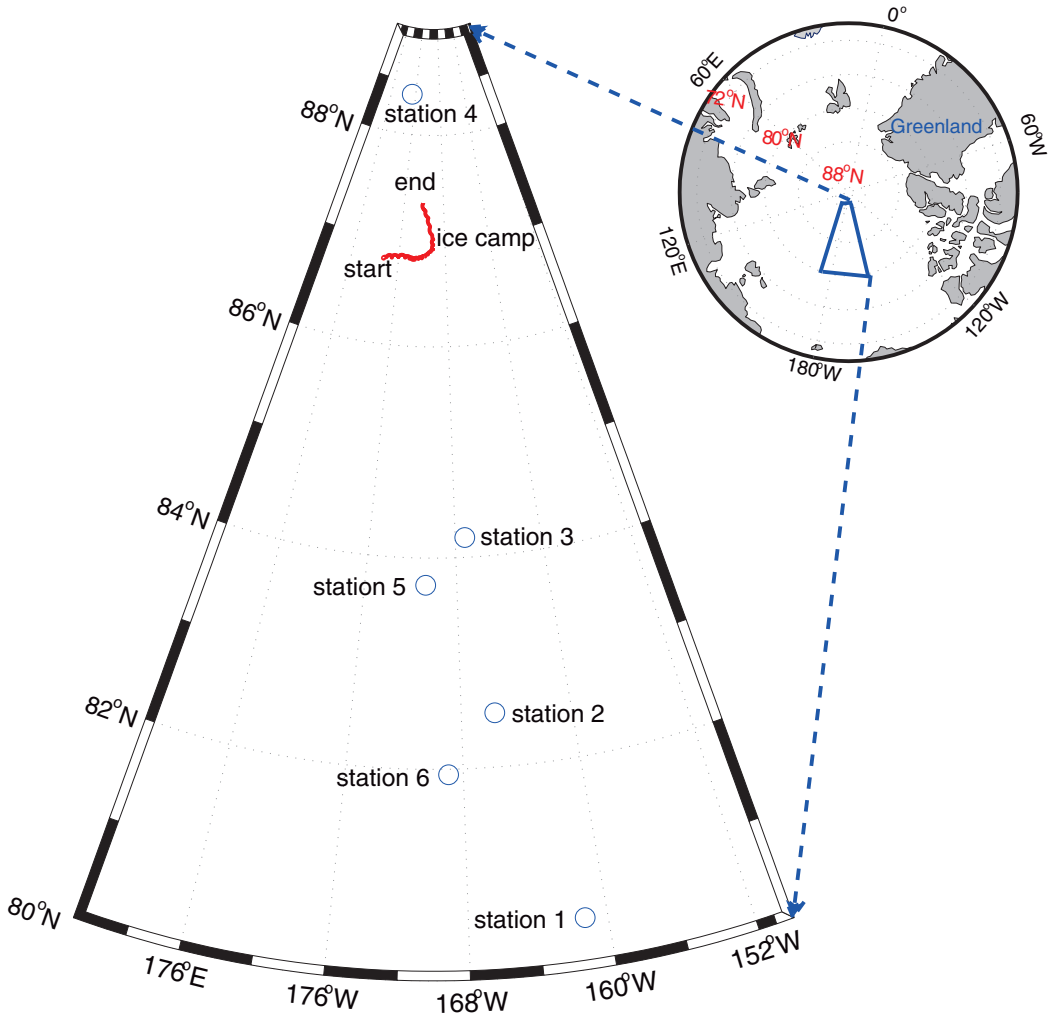

Fig. 1 Locations of ice stations and the ice camp.

irradiances, respectively. The vertical distance from the collector of the downward-looking sensor to the snow surface was 1 m for all measurements. The measurement was made over a representative site with horizontally homogeneous snow cover. The apparatus was assembled away from the final measurement site, and then moved to the measurement site to ensure that the downward-looking sensor would collect more than 96% of the signal from an undisturbed area. If the solar disk was visible, the bar was assembled with sensors extending in the direction perpendicular to the solar azimuth angle, ensuring that no other obstacles, such as high ice ridges or the camp, cast shadows on the measurement site. Measurements at all stations lasted more than 1.5 h with a sampling interval of 10 min.

Three sea-ice cores were collected, while a snow-pit measurement was performed relating to all short-term optical measurements. One core was extracted to measure sea-ice temperature and salinity. Ice temperature was recorded at the interval of 10 cm along the ice core immediately after sampling, using a JUMO Pt-100 needle probe (Dalian, China) accurate to 0.1°C. The core was then cut lengthwise to obtain vertical sections that were 0.05–010 m thick, which were placed in plastic boxes. Sea-ice salinity was measured using a portable WTW conductivity meter (Munich, Germany) accurate to ± 0.5 PSU after ice samples melted completely. The second ice core was used to measure ice density employing a volume method in a cold laboratory onboard the *Xuelong*. The third core was sliced into thin sections with thickness less than 1 mm for crystal structure analysis. The crystal structure is visible between cross-polarized sheets. The brine and gas contents of sea ice were determined according to the equations proposed for sea ice with low salinity and high temperature by Leppäranta & Manninen (1988). The snow-pit measurement included

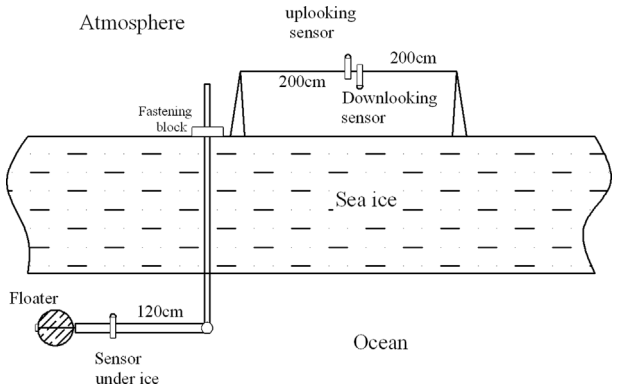

Fig. 2 Schematic diagram of the setup of three RAMSES sensors for measurements of spectral reflection and transmission.

observations of snow temperature, density and stratigraphy. Snow temperature at varying depths was determined using a JUMO Pt-100 needle probe. Snow density was obtained by weighing a defined volume of the snow sample. Snow grain size and structure were determined with a handheld lens and a millimetre-grid sheet.

Ice-camp observations. The ice camp was set up on 8 August at 86.8°N, 179.2°W, and drifted to 87.3°N, 179.2°W by 18 August. Ice-camp observations allowed investigation of processes. A full set of optical measurements, including observations of spectral reflectance and under-ice spectral transmittance, was made at the camp. The setup for the spectral reflectance measurement was the same as that for the short-term measurements. Transmitted irradiance under ice cover was measured by lowering a RAMSES sensor mounted to the end of a hinged arm down a borehole through the ice cover. This below-ice sensor was deployed 10 m aside of the above-surface installation, but still under similar snow and ice, which minimized the effect of shadows on the reflectance measurement and the disruption of the surface during the deployment to insignificant levels. A floater also mounted to the end of the hinged arm under the ice ensured the collector of the below-ice sensor looking vertically upward. The distance from the sensor to the ice bottom was 0.2 m and that from the sensor to the borehole was 1.2 m (Fig. 2). Thus, compared with that setting up the sensor directly under the ice through the borehole, our design reduces the influence of the borehole on the irradiance transmission, especially in the case that the borehole does not completely refreeze during the measurement. Full broadband incident and reflected irradiances were measured with a pair of upward- and downward-looking Kipp & Zonen CM 22 pyranometers (Delft, The Netherlands), which were deployed 30 m aside of the installation for spectral irradiance measurement, over similar smooth snow cover. The apparatus for spectral/broadband irradiance measurements was set up on 8 August and retrieved on 18 August. The sampling intervals were 10 min for the spectral measurements and 2 min for the broadband measurements. Owing to technical problems with the data logger, we did not gain a series of uninterrupted data, especially for the spectral reflection measurement. However, we still acquired a full picture of the temporal changes in vertical partitioning of solar radiation from the atmosphere to the upper ocean from the in situ data.

An ultrasonic rangefinder (Wuhan University, Wuhan, China) was used to monitor the variation in the ice bottom. This sensor, accurate to ± 0.5 cm, was deployed 0.5 m beneath the ice bottom using a frame similar to that for the under-ice spectral installation. The site for the ice-bottom mass balance measurement was located 10 m aside of the above-surface spectral installation, and 12 m aside of the under-ice spectral installation. The three types of sensor were deployed in a triangular form. The initial ice thickness, freeboard and snow depth at the measurement site for the ice-bottom mass balance were 1.68 m, 0.11m and 0.09 m, respectively, while those at the borehole of the under-ice spectral installation were 1.66 m, 0.11 m and 0.09 m, respectively. It therefore makes sense to suppose that the investigation area has the same melt rate at the bottom during the measurement. A mast was set up 40 m from the spectral measurement to monitor the surface air temperature, relative humidity and wind speed and direction at varying heights from 0.5 to 10.0 m.

Two ice-core groups (both with three full-length cores) for measurements of sea-ice temperature, salinity and density. The first group was collected on 14 August and the second one was collected 17 August. One additional ice core collected on 14 August was used for crystal structure analysis. All ice cores were collected approximately 25 m from the spectral installation. Snow-pit measurement was performed 15 m from the spectral installation every one or other day by excavating a new snow pit from the undisturbed area each time. In addition to the measurements carried out at the short-term stations, relative humidity in volume at a depth 2 cm above the snow bottom was determined using a Toikka snow fork with exposed probes (Espoo, Finland). This type of fork is more reliable than its former model because it does not compress the snow pack.

Since both short-term ice stations and the ice camp were located in a relatively narrow meridional sector

Citation: *Polar Research* 2012, *31*, 17325, DOI: 10.3402/polar.v31i0.17325

ranging from 161.33°W to 179.21°W, the local time of UTC—12 h was used for all data collections.

Data processing

All spectral data recorded by the RAMSES sensors were recorded as raw data in counts per channel. Thus, all data were calibrated to absolute spectra and interpolated to a 1-nm grid. Furthermore, before calculating ratios of spectra recorded by different sensors, all RAMSES sensors were mutually calibrated after the fieldwork by setting them to measure incident irradiance synchronously. The reflected and transmitted spectra were corrected for shadow effects independent of wavelength and time, employing the strategy of Nicolaus, Hudson et al. (2010). For our platform, the scaling factors were 1.089 and 1.010, respectively, for the reflected spectrum and the transmitted spectrum. Because of an unexpected variability and a high noise level for the lower end of the spectral ranges from 320 to 350 nm, and the higher end from 920 to 950 nm, we limit the spectrum to 350 to 920 nm to calculate ratios of spectra recorded by different sensors. Owing to the oxygen absorption lines around 760 nm, there were some spikes in the spectral albedo at 750–775 nm. To remove this effect, the spectral albedo was smooth from 750 to 775 nm by linear interpolation.

The vertical co-ordinate from the surface of the ice/snow sheet is denoted z, with a sign convention such that downward is positive. Spectral albedo $\alpha(\lambda)$ is defined as the ratio of the upwelling irradiance above the snow cover $F_r(0, \lambda)$ to the downwelling irradiance above the snow cover $F_d(0, \lambda)$. Spectral transmittance $T(\lambda)$ of the combined snow and sea ice layer is defined as the ratio of the downwelling irradiance immediately beneath the ice cover $F_d(h, \lambda)$ to $F_d(0, \lambda)$, where h is the total thickness of snow and ice. Similarly, the broadband albedo for the whole solar spectrum can be estimated from the pyranometers measurements. The broadband integrated albedo and transmittance from λ_1 to λ_2 are defined as

$$\alpha_{\lambda_1\text{-}\lambda_2} = \frac{\int_{\lambda_1}^{\lambda_2} \alpha(\lambda) F_r(0,\lambda) d\lambda}{\int_{\lambda_1}^{\lambda_2} F_d(0,\lambda) d\lambda}, \quad (1)$$

and

$$T_{\lambda_1\text{-}\lambda_2} = \frac{\int_{\lambda_1}^{\lambda_2} T(\lambda) F_d(h,\lambda) d\lambda}{\int_{\lambda_1}^{\lambda_2} F_d(0,\lambda) d\lambda}. \quad (2)$$

Net absorption irradiance at wavelength λ by the combined snow and sea-ice layer is calculated as

$$F_{abs}(\lambda) = F_d(0,\lambda) - F_r(0,\lambda) - F_d(h,\lambda). \quad (3)$$

As the RAMSES sensor covers the spectrum from ultraviolet A (UV-A) to near infrared, some representative integrated parameters for interesting spectral bands are also calculated and discussed in this study, e.g., the 320(350)–400 nm band relating to the UV-A spectrum, the 400–700 nm band relating to PAR and approximately to visible spectrum, and the 700–920(950) nm band relating to part of near-infrared spectrum.

Results

Sea-ice/snow conditions and spectral albedo at short-term stations

Table 1 summarizes the general descriptions of the short-term measurements and key statistical parameters of the spectral albedo. The spectral albedo recorded at all stations distinctly decreased as the wavelength increased (Fig. 3), especially above 700 nm, i.e., for the near-infrared spectrum $\alpha_{350\text{–}920}$ ranged from 0.73 to 0.88, which can be treated as a representative value for snow-covered ice (Perovich 1998). The maximum spectral albedo ranged from 0.81 to 0.96, which appeared in the UV-A or violet spectrum. The snow covers at stations 1 and 3 had similar depth and textural structure. Both had relatively dry fresh snow of fine dendritic grain over the surface and a gradual increase in grain size from top to bottom. The fresh-snow layers there produced a flatter spectrum of albedo compared with other cases. At station 1, however, the fresh-snow layer on the surface was thicker than that at station 3 (ca. 0.8 cm vs. ca. 0.4 cm). This associated with a larger grain size for the whole depth, are the most probable reasons for the larger albedo for the whole spectrum measured at station 1. Although there was a thin slush layer of 1.0 cm between the snow and sea ice at station 1, there was no marked depression for the near-infrared albedo. This implies that the snow cover there was optically thick, resulting in an abundant backscattering to the atmosphere. It also reduced the spectral absorption of the water content in the underlying slush layer for the near-infrared region. The cases for stations 5 and 6 differed from the case for station 1. As the snow layers at stations 5 and 6 were thinner, more irradiation was transmitted to the snow bottom. Thus, the thin slush layers there, with depth of 1.0 cm, absorbed marked near-infrared irradiance, which significantly depressed the near-infrared albedo. Station 4 had a spectral albedo similar to that at station 1 below 750 nm. However, above this wavelength, the spectral albedo at station 4 increasingly deviated from that at station 1. This can be attributed

Table 1 General description of short-term measurements and statistical parameters of spectral albedo.

	Station 1	Station 2	Station 3	Station 4	Station 5	Station 6
Lat. (°N)	80.49	82.51	84.19	88.38	83.74	81.95
Long. (°W)	161.33	165.60	167.12	177.17	170.69	169.00
Time	1 Aug. 9:20–10:20	3 Aug. 9:10–10:10	4 Aug. 12:30–14:00	19 Aug. 15:00–16:00	22 Aug. 18:10–19:10	23 Aug. 14:00–15:25
Solar elevation angle (°)	21.4–23.0	22.7–24.7	23.0–23.2	13.7–14.0	10.7–12.7	17.3–18.8
T_a (°C) [a]	0.5	−0.2	−1.6	−0.2	−1.5	0.4
Cloudiness (tenth)	10 (solar disk is invisible)	8 (solar disk is visible)	8 (solar disk is visible)	2 (clear sky)	6 (solar disk is visible)	1 (clear sky)
h_s (cm) [b]	11.0	15.0	12.5	11.5	7.5	7.0
h_{sl} (cm) [c]	1.0	0.5	–	–	1.0	1.0
T_s(°C) [d]	−0.1	−0.1	−0.2	−0.1	−0.2	−0.1
h_g+h_c (cm)[e]	20+120	30+145	21+104	14+113	13+111	7+82
Freeboard (cm)	16	15	6	6	9	7
T_i (°C) [f]	−0.38	−0.28	−0.46	−0.38	−0.38	−0.36
S_i (PSU) [g]	0.52	0.32	0.98	0.59	0.86	0.7
ρ_i (g cm^{-3}) [h]	811	750	794	784	796	754
$\upsilon_a+\upsilon_b$ (%)[i]	12.1+6.2	18.6+4.7	14.3+9.4	15.1+6.7	14.1+10.0	18.5+8.1
$\alpha_{350–920}$	0.85	0.88	0.81	0.85	0.82	0.73
$\alpha_{400–700}$	0.88	0.92	0.83	0.88	0.87	0.77
Max. albedo	0.89	0.96	0.84	0.90	0.91	0.81
$\alpha_{900}/\alpha_{500}$	0.87	0.80	0.86	0.81	0.69	0.75

[a]Surface air temperature at altitude of 1 m.

[b]Snow depth.

[c]Depth of slush layer between snow and ice.

[d]Temperature at snow bottom.

[e]h_g is thickness of top granular ice layer; h_c is thickness of column ice layer at bottom.

[f]Mean sea-ice temperature of top 50-cm layer.

[g]Mean sea-ice salinity of top 50-cm layer.

[h]Mean sea-ice density of top 50-cm layer.

[i]υ_a is bulk gas content (volume) for top 50-cm layer; υ_b is bulk brine content (volume) for top 50-cm layer.

Citation: *Polar Research* 2012, 31, 17325, DOI: 10.3402/polar.v31i0.17325

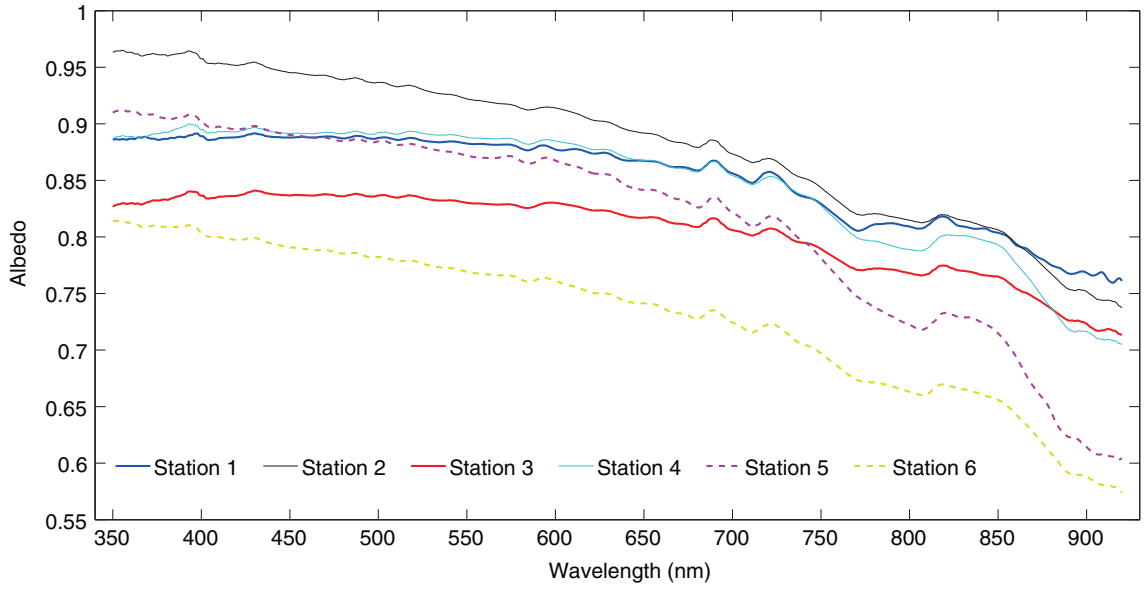

Fig. 3 Spectral albedo from 350 to 920 nm recorded at the short-term ice stations.

to there being no dry new snow on the surface and the snow cover being relatively wet at station 4, resulting in large absorption for the near-infrared spectrum. Station 2 had snow cover with the largest depth, and therefore the largest value of $\alpha_{350-920}$. The high-level spectral albedo there was more outstanding for UV-A and the visible spectrum than for the near-infrared spectrum. It also could be attributed to the stronger spectral absorption of a thin slush layer between snow and ice for the near-infrared spectrum. The ratio between α_{900} and α_{500} represents the spectral shape of albedo and the absorption ability of liquid water within snow cover to a large degree (Nicolaus, Gerland et al. 2010). This ratio ranged from 0.69 to 0.87 in our measurements, which could be related to the melting phase of snow cover following the definition of Nicolaus, Gerland et al. (2010). Low values of this ratio were recorded at stations 5 and 6, which could be attributed to the more advanced melt of snow cover there. After removing the snow cover for the snow-pit measurement, a thin water film appeared over bare ice at stations 5 and 6, but not other stations.

Ice-core measurements showed that the ice covers of all stations had large gas content. This was noted especially at stations 2 and 6, where the full-length mean ice temperatures were warmer and intense desalination had occurred. Air bubbles strengthen the scattering of solar irradiation transmitted through an ice column. However, compared with snow cover, the geophysical properties of sea ice (including sea-ice thickness, the thickness of the top granular ice layer, and the gas content) did not have any identifiable effect on the surface spectral albedo, which implied that the snow covers at all stations were still optically thick, even though all were in the melting stage.

However, melt ponds were developed over some parts of all investigated floes, with coverage ranging from 10% to 25%. Around some of these melt ponds snow-free areas of sea ice had developed. However, the coverage of bare sea ice was negligible. The albedo of melt ponds ranges from 50% to 75% of that of snow-covered ice, depending on the depth of the pond water and bottom sea ice (Perovich et al. 2002). The spatial integrated albedo of the investigated floes can be estimated as:

$$\bar{\alpha} = A_p\alpha_p + A_i\alpha_i + A_s\alpha_s, \quad (4)$$

where $\bar{\alpha}$ is the spatial integrated albedo of the investigated floe, A_p, A_i and A_s are the coverage of melt pond, bare sea ice and snow-covered sea ice, α_p, α_i and α_s are the albedos of melt pond, bare sea ice and snow-covered sea ice (Perovich 2005). Melt ponds therefore depressed the spatial integrated albedo by about 2.5–12.5% for our investigated floes.

Weather, sea-ice and snow conditions at the ice camp

The sky was mostly overcast throughout the camp period. The solar disk was visible completely for only a few hours on 8, 14, 16 and 18 August, providing relatively high levels of incident global radiation on these occasions. There were several minor snowfall events during the camp period (Fig. 4a). There was an event of

slight drizzle during a period of slightly warmer air temperatures from the afternoon of 16 August to the early morning of the following day. Three distinct phases can be identified from the surface air temperature (Fig. 4b). Phase I (before noon on 12 August) was characterized by a stable moderate air temperature ranging from −2.8°C to −0.1°C and having a mean value of −1.0±0.6 °C. Phase II was from 12 to 16 August. The surface air temperature steadily decreased during the initial part of Phase II, and reached a low of −4.5°C by the morning of 15 August. Thereafter, the temperature increased again and reached 1.4°C by the afternoon of 16 August, at which time Phase III commenced. Phase III was characterized by a stable warm air temperature with a mean value of 0.6±0.6°C. The solar elevation angle ranged from 10.5° to 19.7° during the measurement period, which was comparable to the range for the short-term measurements.

No distinct change was observed for the snow depth at our investigated site before 17 August. However, the textural structure of the snow cover slightly changed (Fig. 4d). Thin fresh snow layers appeared over the surface on 10, 11 and 16 August, owing to snowfall events. These fresh-snow layers disappeared in one or two days after the snowfall, as the snow grain size increased owing to the melting and sintering snow grains. A thin icy layer appeared between the snow and ice on 14 August, owing to the refreezing of snowmelt there. As the freeboard of the sea-ice cover was positive, we suppose that this icy layer was superimposed ice and consisted only of freshwater ice. This superimposed ice layer survived until 18 August, when it melted into slush owing to the marked increasing temperature at the snow bottom. The wetness (relative humidity in volume) at a depth of 2 cm above snow bottom did not distinctly change until 13 August. It decreased to a minimum of 1.88% by 14 August with the formation of the superimposed ice there. Thereafter, it increased again and reached a maximum by 18 August with the formation of a slush layer.

The sea-ice bottom decayed by 5.3 cm from 9 to 18 August, with a mean melt rate of 0.5±0.2 cm·d^{-1}. The temporal function of the ice-bottom-melt rate was close to that of the surface air temperature. The latter can explain 39% of the former at a significance level of 0.0001. As shown in the photographs of the thin ice segments (Fig. 5), the top 0.13 m layer was granular ice. Beneath this layer, the columnar congelation ice was 1.53 m thick. The grain size was about 2–3 mm at the top of the granular ice layer, and about 5–10 mm at the bottom of this layer. The crystal size of the columnar ice layer also increased distinctly from top to bottom. As there was no distinct discontinuous layer anywhere within the columnar ice layer, we supposed that the investigated floe was first-year ice. Comparison between ice cores collected on 17 August and those collected on 14 August indicates an increase in sea-ice temperature and brine drainage (Fig. 6), resulting in an increase in gas content and a decrease in ice density

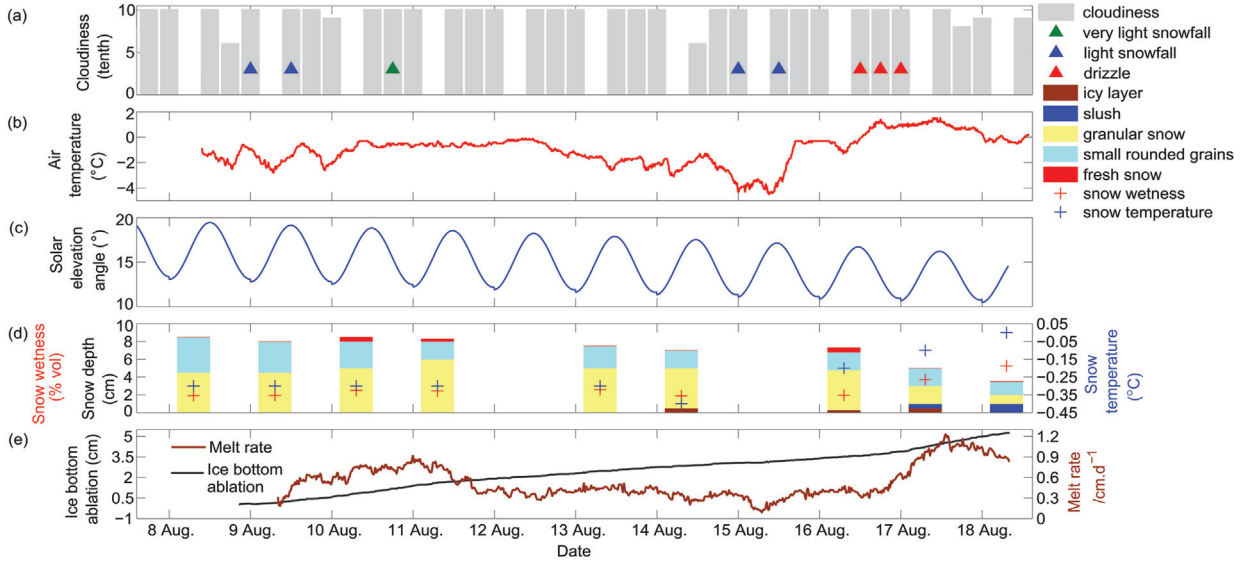

Fig. 4 (a) Cloudiness and records of key synoptic events, (b) variations in surface air temperature at altitude of 1 m, (c) variations in solar elevation angle, (d) variations in the textural structure of snow cover, temperature at the snow bottom and wetness at a depth 2 cm above the snow bottom and (e) ablation of the sea-ice bottom and its rate.

Citation: *Polar Research* 2012, *31*, 17325, DOI: 10.3402/polar.v31i0.17325

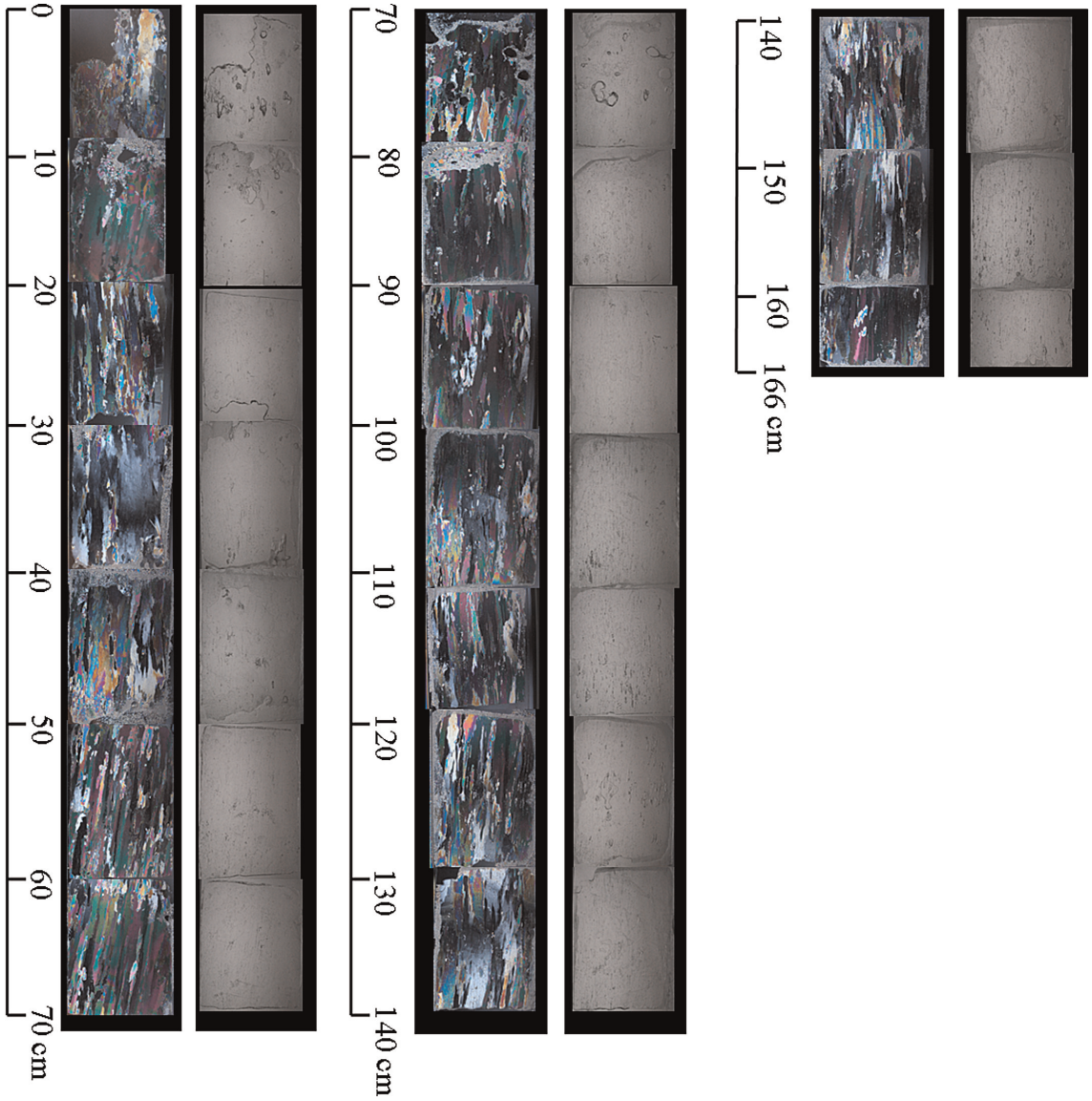

Fig. 5 Thin sections of the sea-ice core collected on 14 August at the ice camp under polarized light and natural light.

(Table 2). Since the amount of solid crystals within sea ice is negligible when ice temperature is higher than -4°C (Cox & Weeks 1983), the interior melt of sea ice can be characterized by the change in ice porosity υ, which is the summation of brine content and gas content ($\upsilon = \upsilon_a + \upsilon_b$). The equivalent latent heat corresponding to the interior melt of sea ice, F_{ice}, can be estimated as

$$F_{ice} = \frac{dv}{dt}\rho_i h_i L_i, \quad (5)$$

where ($d\upsilon/dt$) is the change rate of ice porosity, h_i is sea-ice thickness and L_i is sea-ice latent heat of fusion. Thus, the temporal mean F_{ice} from 14 to 17 August was 22.0 $W \cdot m^{-2}$.

Spectral albedo and transmittance at the ice camp

Figure 7 presents the incident and reflected spectral irradiances over the snow surface, the downward spectral irradiance immediately under the ice, and the calculated spectral albedo and transmittance. Both the reflected spectrum over the snow surface and the transmitted spectrum under the ice contained a strong daily signal as the incident spectrum did. The spectral albedo remained steady and high until 17 August, when it commenced a rapid decrease due to the melt of snow (Fig. 4d). There

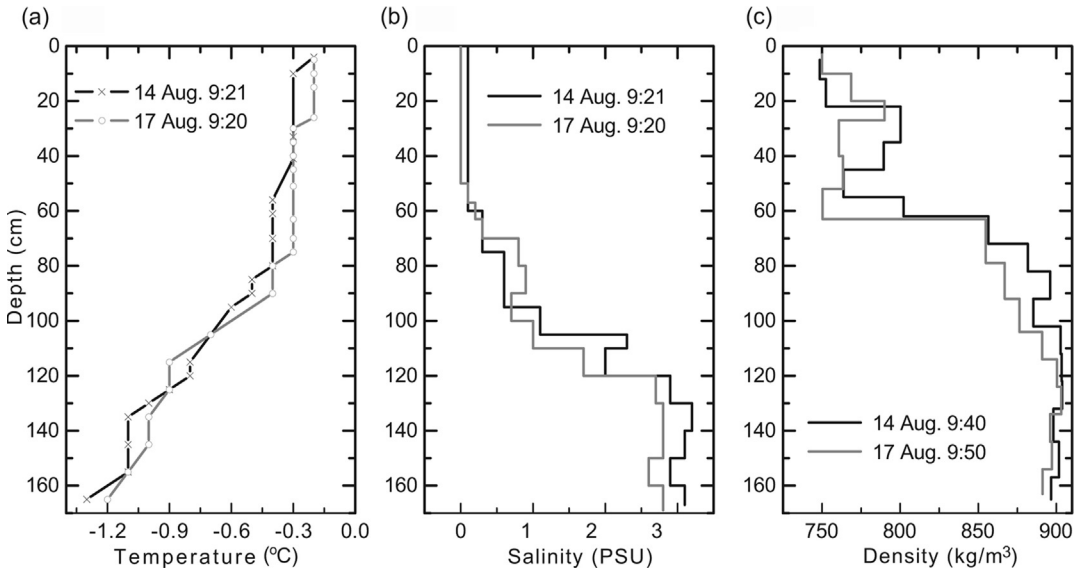

Fig. 6 Sea-ice temperature, salinity and density profiles of the ice cores collected at the ice camp.

was a temporal depression in the spectral transmittance from the morning of 9 August to the morning of 10 August (Fig. 7e), which relates to the appearance of a thin fresh snow cover on the surface at that time (Fig. 4d). However, no effect of this fresh snow cover on the full-broadband albedo can be identified. As the fresh snow cover was thin and had large spatial inhomogeneity, there should be no (or only much thinner) fresh snow over the footprint of the full-broadband albedo measurement on that occasion in all probability. This was attributable to the spatial disparity of the surface albedo. The broadband albedo measured by pyranometers was less than $\alpha_{350–920}$ measured by RAMSES sensors for most of the measurement period (Fig. 8a), as the former included a stronger signal in the near-infrared region, where the albedo was relatively low. The temporal variability in $\alpha_{350–920}$ can explain 74.5% of that in the broadband albedo at a significance level of 0.0001. This value is lower than the result reported by Nicolaus, Gerland et al. (2010) owing to the footprints of the two measurements almost overlapping in their case. The spectral transmittance increased gradually from 17 August owing to the melting of snow and sea ice. Because the snow geophysical properties in the melting stage had complex temporal variation and the albedo had a stronger relationship with the snow geophysical properties, the albedo had greater temporal fluctuation compared with the transmittance. There were two episodic troughs for the spectral albedo in the late afternoon of 17 August and the very early morning of 18 August (Fig. 8a). These episodic functions were filtered in the time series of spectral transmittance to a high degree, but were still identifiable (Fig. 9a). The spectral albedo was high in UV-A and visible regions and low in near-infrared region. This discrepancy increased remarkably from 17 August onward, owing to the larger absorption of near-infrared irradiance due to melting snow. This resulted in a distinct depression of the ratio between $\alpha_{700–920}$ and $\alpha_{400–700}$ (Fig. 8b). This ratio also depended on the value of $\alpha_{350–920}$. A large $\alpha_{350–920}$ related to a large ratio between $\alpha_{700–920}$ and $\alpha_{400–700}$. Their Pearson correlation coefficient was 0.964, which was statistically significant at a level of 0.0001. This can be explained by a lower $\alpha_{350–920}$ relating to advanced snow melting, which would increase the water content within/under the snow cover and further accelerate absorption of near-infrared irradiance. We therefore suppose that snowmelt first decreases the near-infrared albedo and then the whole broadband albedo, which has also been observed by Gerland et al. (1999) for first-year ice in an Arctic

Table 2 Statistical parameters of the full-length ice cores collected at the ice camp.

Sampling date	Mean temperature (°C)	Mean salinity (PSU)	Mean density ($kg \cdot m^{-3}$)	Mean porosity, $v_a + v_b$ (%)
14 August	−0.65	1.24	851	8.1+9.1
17 August	−0.51	1.12	839	9.4+10.2

Citation: *Polar Research* 2012, *31*, 17325, DOI: 10.3402/polar.v31i0.17325

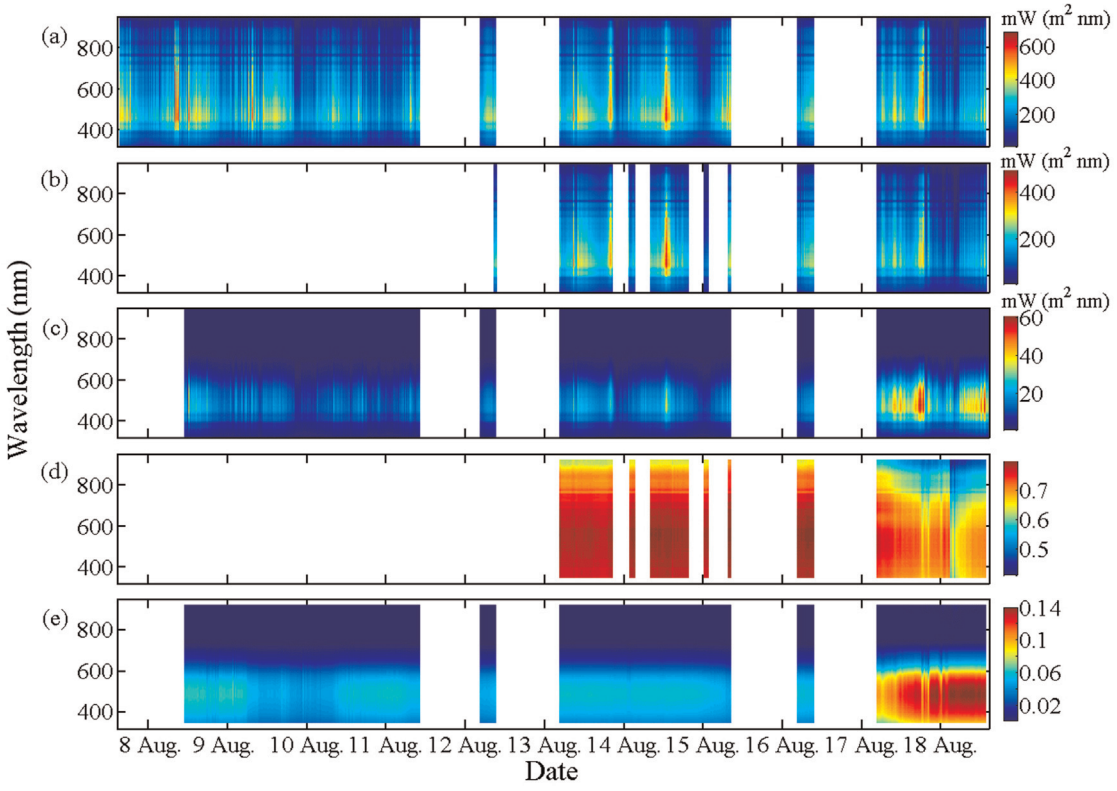

Fig. 7 Temporal variations in (a) incident, (b) reflected and (c) transmitted spectral irradiance and spectral (d) albedo and (e) transmittance.

fjord. Since snow melted more rapidly from 17 August, the near-infrared albedo played a weaker role in determining the integrated value, while the near-infrared transmittance played a stronger role in determining the integrated value compared with the case for the former period (Figs. 8b, 9b). This was the largest contribution of the snowmelt to the wavelength dependence of albedo and transmittance. The integrated transmittances in varying spectral regions had similar temporal dependence, which resulted in relatively steady ratios among the integrated values of varying spectral regions. The ratio between T_{600} and T_{450} is a sensitive indicator of biomass (Perovich et al. 1993). This ratio decreased gradually until 17 August, and then climbed again. The former decrease can be attributed to the ice-bottom melting, which could have dropped some biomass into the water. The later increase can be attributed to the increasing PAR available at the ice bottom.

Spectral albedo had weak wavelength dependence below 700 nm (Fig. 10a). The wavelength dependence was strengthened gradually above 700 nm, especially after 17 August. There was a steady peak value in spectral transmittance at 478 ± 5 nm (Fig. 10b). Spectral transmittance decreased rapidly at longer wavelengths as the absorption by ice and snow increased. At shorter wavelengths, there was less wavelength dependence. According to the peak value of spectral transmittance, there was a steady trough at about 500 nm in the spectral absorption of the combined layer of snow and ice. Note that the spectral absorption shown in Fig. 10c is defined as the ratio between the irradiance absorbed by snow and ice and the incident irradiance. Above the green wavelengths, the spectral absorption increased rapidly as wavelength increased. Compared with the surface spectral albedo, the spectral absorption had a greater effect on the wavelength dependence of the spectral transmittance, especially for the near-infrared region and for measurements after 17 August.

Discussion

Generally, our measured albedo can be divided into three gradations. In the first group are stations 1, 2 and 4, which had high albedos because observations were carried out relatively early at these stations or they were located at relatively high latitudes. Stations 3 and 5, with moderate albedo, belong to the second group. The ice-camp measurement showed a clear temporal process of snow melting and albedo decreasing. The initial wavelength-dependence pattern of spectral albedo was

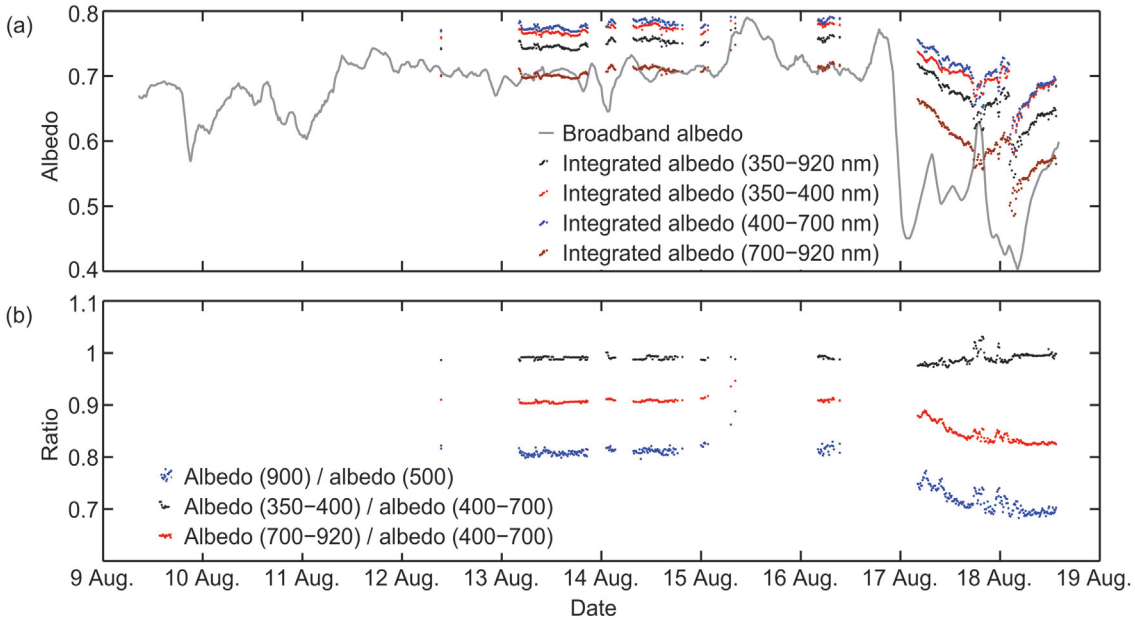

Fig. 8 (a) Temporal variations in the integrated albedo of varying wavelength ranges and the full-broadband albedo measured by pyranometers, and (b) ratios between α_{900} and α_{500}, between $\alpha_{350–400}$ and $\alpha_{400–700}$ and between $\alpha_{700–920}$ and $\alpha_{400–700}$.

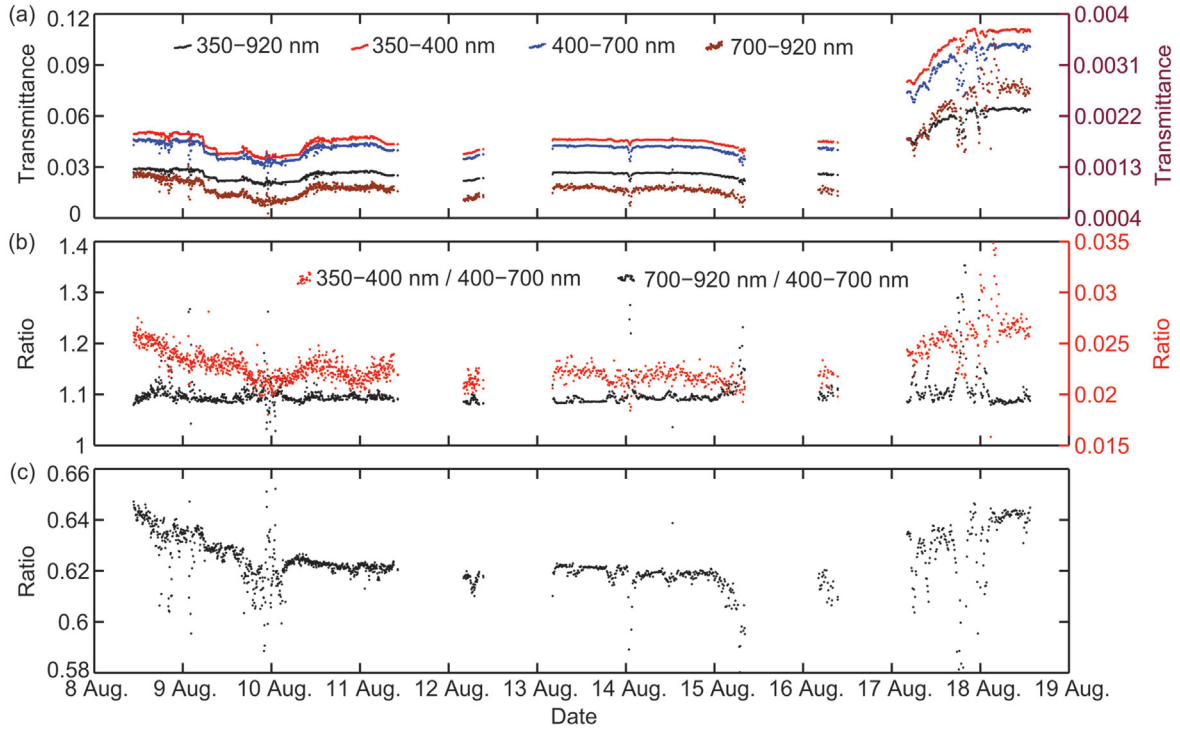

Fig. 9 (a) Temporal variations in integrated transmittance of varying wavelength ranges (note that $T_{700–920}$ refers to the right y-axis, which has a different scale), (b) the ratios between $T_{350–400}$ and $T_{400–700}$ and between $T_{700–920}$ and $T_{400–700}$, with the latter referring to the right y-axis with different scale and (c) the ratio between T_{600} and T_{450}.

Citation: *Polar Research* 2012, *31*, 17325, DOI: 10.3402/polar.v31i0.17325

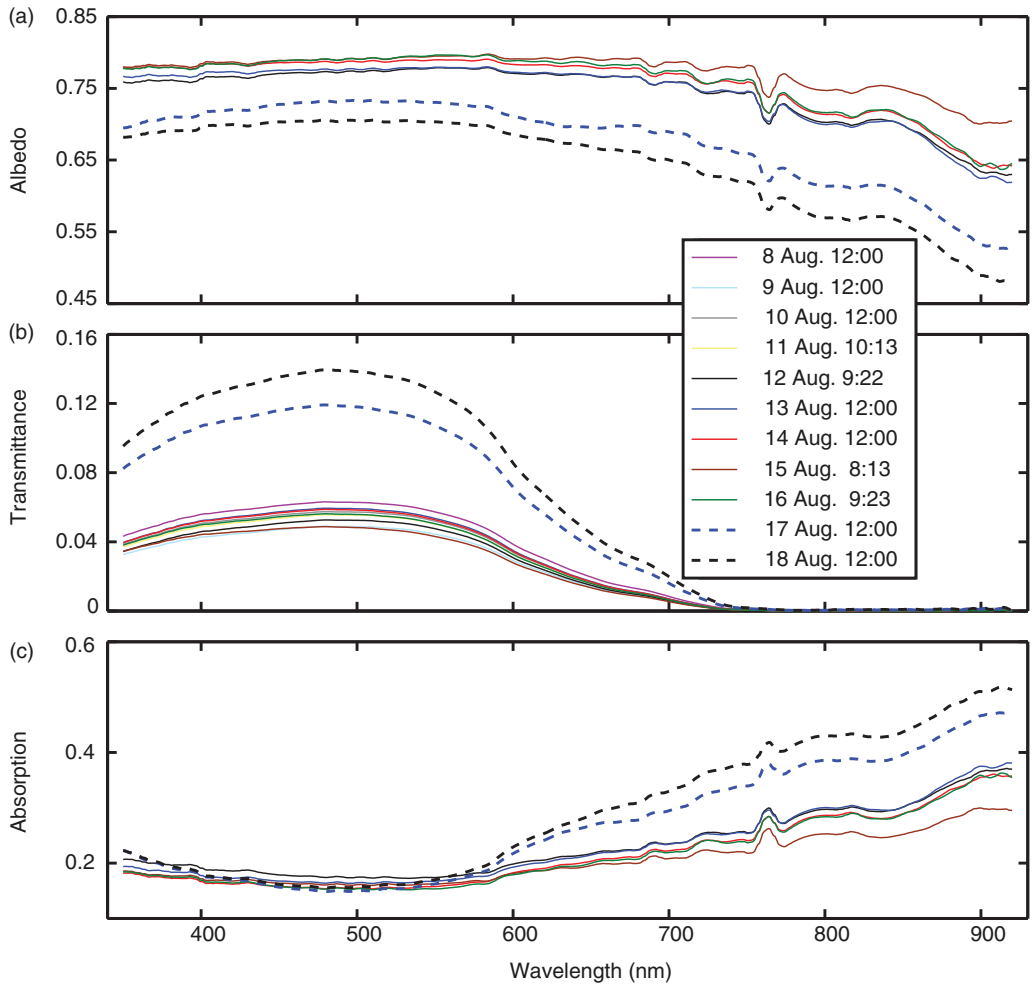

Fig. 10 Spectral (a) albedo, (b) transmittance and (c) absorption at the ice camp.

similar to that at station 3, but with a relatively low value (0.74 vs. 0.81). This can be attributed to the snow covers at the two stations having similar textures and the station 3 having a relatively thick snow cover. By the end of the camp period, the spectral albedo had a pattern of wavelength dependence similar to that at station 6. The patterns related to the advanced phase of snow melting. The ice camp and station 6 therefore comprise the third group.

Because our measurements were very limited, we cannot gain a full picture of surface albedo for the whole High Arctic from our measurements. The CHINARE-2010 cruise also involved helicopter-based spectral albedo observations using ASD spectrometers (Boulder, Co, USA). These measurements are able to extend ice-based results to a regional scale (Pedersen et al. 2009), i.e., to obtain the aggregate-scale albedo and to estimate the contributions of leads and melt ponds to the aggregate-scale albedo for the complex Arctic surface in summer. This is of special importance from a climatology perspective (Perovich 2005; Lu et al. 2010). These data are still being processed, and the results will complement the present study.

Melting of snow and sea ice will heighten the irradiance transmittance through snow-covered ice and accelerate the disposal of solar radiation into the upper ocean, which will in turn accelerate ice-bottom melting. Similarly, owing to the melting of snow and ice, a column of snow and sea ice will have greater water content in the form of slush or brine inclusions, which will accelerate irradiance absorption by snow and ice and further accelerate interior melting of snow and ice. Figure 11 illustrates the partitioning of incident solar irradiance among reflection to the atmosphere, absorption by snow and ice, and transmission to the ocean and the equivalent latent heat flux corresponding to ice-bottom ablation at the ice camp. After the snow cover melted rapidly from 17 August onward, both the irradiance absorbed by the

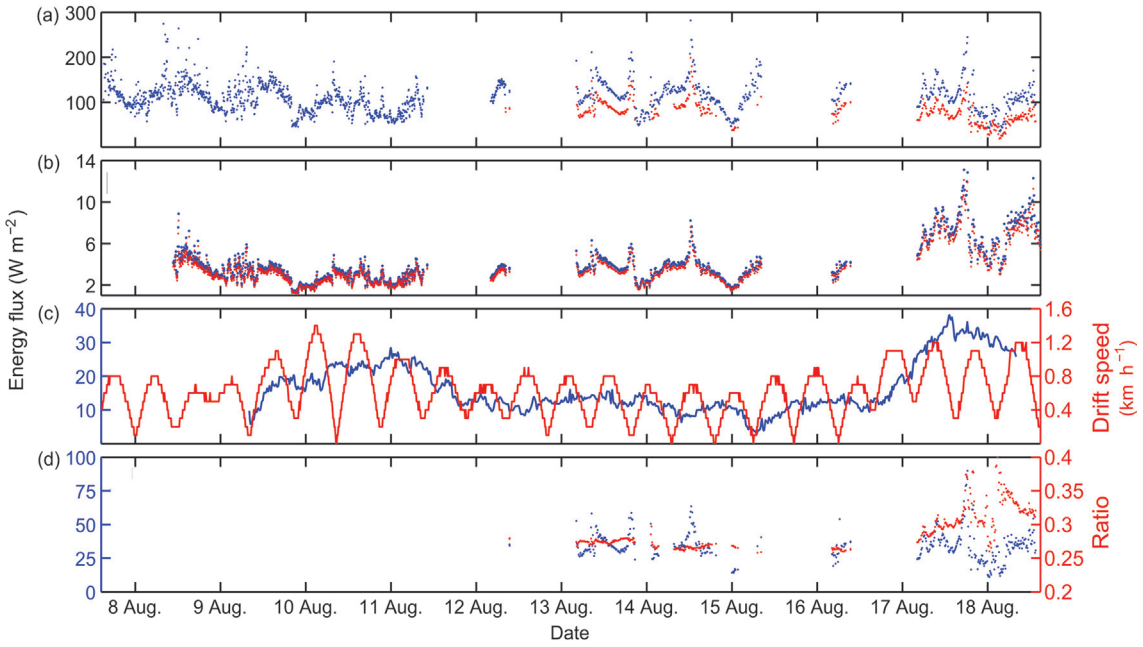

Fig. 11 (a) Integrated incident (blue) and reflected irradiances (red) over the snow surface at 320–950 nm, (b) downward irradiances under the ice at 320–950 nm (blue) and 400–700 nm (red), (c) equivalent latent heat flux of ice-bottom ablation (blue) and drift speed of the camp (red, referring to the right y axis), and (d) irradiance absorbed by snow and ice at 320–950 nm (blue), and its ratio compared with incident irradiance (red, referring to the right y axis).

snow and ice and that transmitted into the upper ocean increased remarkably. Both resulted in less irradiance being reflected back to the atmosphere. The temporally averaged ratio among the reflected, the absorbed and the transmitted irradiance from noon on 13 August to noon the next day was 0.70:0.27:0.03, while that from noon on 17 August to noon the next day was 0.60:0.33:0.07. On average, the transmitted irradiance under the ice at 320–950 nm and that in the PAR region were 3.6 ± 0.9 W·m^{-2} and 3.3 ± 0.9 W·m^{-2}, and 7.2 ± 2.1 W·m^{-2} and 6.5 ± 2.0 W·m^{-2}, respectively, for these two representative temporal intervals previous to and after the onset of rapid snow melting. This implies that the available radiation for oceanic heating and biotical photosynthesis under the ice increased by approximately a factor of 2 in a short period owing to the melting of snow and ice. The temporally averaged value of the transmitted irradiance under the ice at 320–950 nm from noon on 9 August to the morning of 18 August was 3.7 ± 1.8 W·m^{-2}, which was about 19% of the equivalent latent heat flux for the ice-bottom ablation. The oceanic heat flux is the major energy source for ice-bottom ablation in summer, as both the conductive heat flux resulting from vertical ice temperature gradient and specific heat flux resulting from ice warming or cooling at the ice bottom are quite low in the melting phase (Perovich & Elder 2002; Lei et al. 2010). The equivalent latent heat flux for the ice-bottom ablation can represent the aggregate-scale solar radiation absorbed by the upper ocean to a large degree. We thereby infer that on a regional scale, the irradiance transmitted through snow-covered ice was low compared with that transmitted through bare ice, ponded ice and open water in summer for the present High Arctic. This is attributable to a low sea-ice concentration and large melt-pond coverage in the region we investigated. The aerial observations showed that the sea-ice concentration and melt-pond coverage were about 70% and 25%, respectively, within a 20 km radius of the ice camp on 18 August. The aerial photograph of the camp floe shot by hand-held camera from helicopter on this day was shown in Fig. 12. The mean drift speed of the camp floe from 8 to 18 August was 0.62 ± 0.26 km/h. The molecular exchange between the ice bottom and upper ocean is strongly affected by the friction velocity (Shirasawa et al. 1997). Thus, the drift speed of the floe can affect oceanic heat flux at the ice bottom. We find that the low frequency variations in the equivalent latent heat flux showed a similar trend as those in the drift speed of the floe (Fig. 11c). The variations in the daily mean drift speed of the floe can explain 62.3% of that in the daily mean value of equivalent latent heat flux for the ice-bottom ablation, which is significant at the level of 0.01. The effect of friction velocity can explain why there were distinct peaks of the equivalent latent heat

Citation: *Polar Research* 2012, *31*, 17325, DOI: 10.3402/polar.v31i0.17325

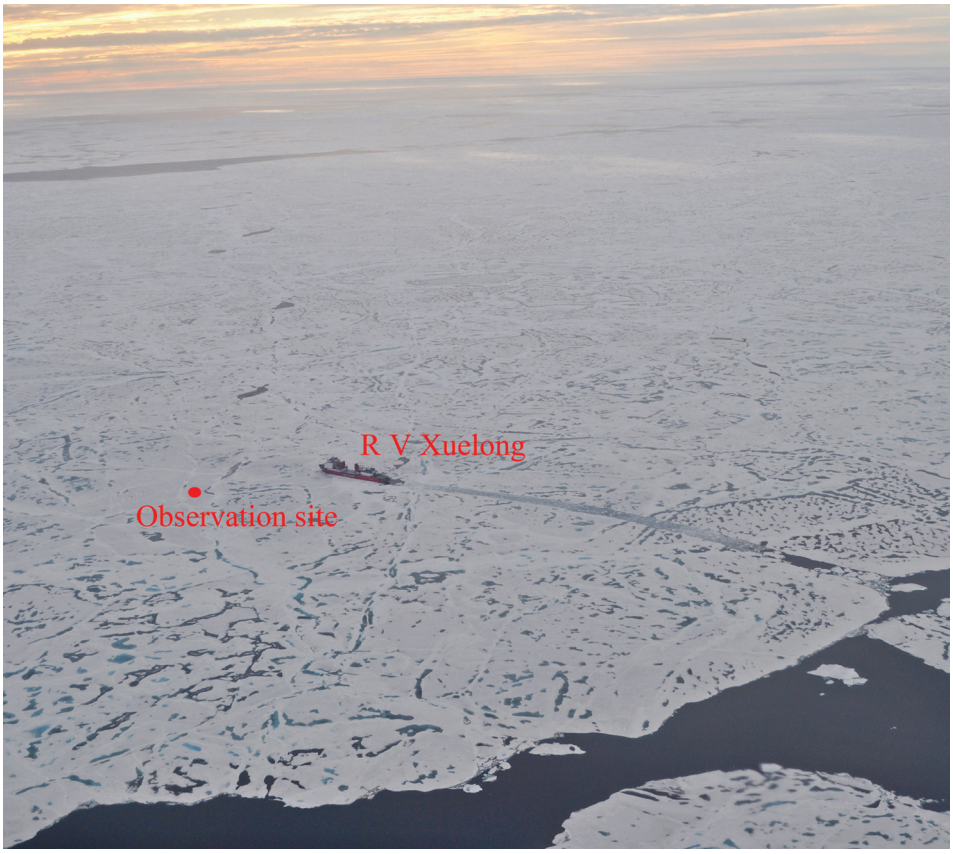

Fig. 12 Aerial photograph of the camp floe on 18 August.

flux for the ice-bottom ablation on around 10 to 11 August and 17 to 18 August (Fig. 11c). However, the peak that occurred on 17 to 18 August was more pronounced due to the significantly increase in the transmitted irradiance under the ice. Generally, the friction velocity and solar radiation transmitted through the ice cover was decisive for the ice-bottom mass balance during the later summer for the areas of the High Arctic investigated. During the duration between the sampling times of the two ice-core groups shown in Fig. 6, the mean irradiance absorbed by snow and sea ice at 320–950 nm was 34.1 ± 9.3 W·m^{-2}, which was 1.6 times of the equivalent latent heat flux corresponding to sea-ice interior melting.

Both our set-up for spectral reflection and transmission measurements and that of Nicolaus, Gerland et al. (2010) were deployed at a manually operated camp, which implies that large logistical support is needed to obtain long-term data. Fortunately, the method of sea-ice optical measurements has been attested to be highly capable of year-round application in the hostile Arctic circumstances (Nicolaus, Gerland et al. 2010). This approach provides the opportunity to employ the spectral measurements in the sea-ice mass balance buoy, to monitor the seasonal variability in vertical solar partitioning from the atmosphere to ocean and to assess its role in the mass balance of the combined snow and sea-ice layer.

Conclusions

In August of 2010, spectral albedo was measured at six short-term ice stations. Snow and sea-ice geophysical measurements were also made at the same sites. All the measured floes comprised first-year ice. Snow cover with a depth ranging from 7.0 to 15.0 cm was still optically thick, but had commenced its melting phase. $\alpha_{350-920}$ ranged from 0.73 to 0.88. The minimum albedo was obtained for the last station, which was measured at 81.95°N on 23 August.

Spectral albedo and transmittance measurements were made over a period of about 10 days at an ice camp. During the observation, $\alpha_{350-920}$ ranged from 0.54 to 0.77, while $T_{350-920}$ ranged from 0.017 to 0.065. There was obvious snow and ice melting from 17 to 18 August due to the warm surface air temperature and an event of

slight drizzle, which changed the partitioning of incident solar irradiance from the atmosphere to ocean to a large degree. Although the incident solar irradiance remained stable during this period, the transmitted irradiance under the ice increased by a factor of 2. Compared with the melting of the sea-ice interior and bottom, the melting of snow had a greater effect on irradiance absorption and transmission, especially for the near-infrared spectrum. More PAR transmitted into the upper ocean under the sea ice related to an increase in the biological mass, which could be identified in our spectral measurements.

Acknowledgements

This work was financially supported by the National Natural Science Foundation of China (grant nos. 40930848 and 41106160), the Shanghai Postdoctoral Sustentation Fund (grant no. 11R21421800), the Norwegian Research Council through support to the Advancing Modeling and Observing Solar Radiation of Arctic Sea Ice project (grant no. 193592/S30), the Chinese Arctic and Antarctic Administration (grant no. IC2010007) and the Academy of Finland (grant no. 122412). We thank Dr Marcel Nicolaus for his suggestions on developing the platform for spectral optical measurements. Two anonymous reviewers are thanked for their comments, which considerably improved this work.

References

Comiso J.C., Parkinson C.L., Gersten R. & Stock L. 2008. Accelerated decline in the Arctic sea ice cover. *Geophysical Research Letters 35*, L01703, doi: 10.1029/2007GL031972.

Cox G.F.N. & Weeks W.F. 1983. Equations for determining the gas and brine volumes in sea-ice samples. *Journal of Glaciology 29*, 306–316.

Ehn J.K., Papakyriakou T.N. & Barber D.G. 2008. Inference of optical properties from radiation profiles within melting sea ice. *Journal of Geophysical Research—Oceans 113*, C09023, doi: 10.1029/2007JC00456.

Gerland S., Winther J.-G., Ørbræk J.B. & Ivanov B. 1999. Physical properties, spectral reflectance and thickness development of first year fast ice in Kongsfjorden, Svalbard. *Polar Research 18*, 275–282.

Grenfell T.C. & Maykut G.A. 1977. The optical properties of ice and snow in the Arctic Basin. *Journal of Glaciology 18*, 445–463.

Inoue J., Kikuchi T. & Perovich D.K. 2008. Effect of heat transmission through melt ponds and ice on melting during summer in the Arctic Ocean. *Journal of Geophysical Research—Oceans 113*, C05020, doi: 10.1029/2007JC004182.

Kwok R. & Rothrock D.A. 2009. Decline in Arctic sea ice thickness from submarine and ICESat records: 1958–2008. *Geophysical Research Letters 36*, L15501, doi: 10.1029/2009GL039035.

Lei R., Li Z., Cheng Y., Wang X. & Chen Y. 2009. A new apparatus for monitoring sea ice thickness based on the magnetostrictive-delay-line principle. *Journal of Atmospheric and Oceanic Technology 26*, 818–827.

Lei R., Li Z., Cheng B., Zhang Z. & Heil P. 2010. Annual cycle of landfast sea ice in Prydz Bay, east Antarctica. *Journal of Geophysical Research—Oceans 115*, C02006, doi: 10.1029/2008JC005223.

Leppäranta M. & Manninen T. 1988. *The brine and gas content of sea ice with attention to low salinities and high temperatures. Report 88–2*. Helsinki: Finnish Institute for Marine Research.

Light B., Grenfell T.C. & Perovich D.K. 2008. Transmission and absorption of solar radiation by Arctic sea ice during the melt season. *Journal of Geophysical Research—Oceans 113*, C03023, doi: 10.1029/2006JC003977.

Lu P., Li Z., Cheng B., Lei R. & Zhang R. 2010. Sea ice surface features in Arctic summer 2008: aerial observations. *Remote Sensing of Environment 114*, 693–699.

Mundy C.J., Ehn J.K., Barber D.G. & Michel C. 2007. Influence of snow cover and algae on the spectral dependence of transmitted irradiance throughn Arctic landfast first-year sea ice. *Journal of Geophysical Research—Oceans 112*, C03007, doi: 10.1029/2006JC003683.

Nicolaus M., Gerland S., Hudson S.R., Hanson S., Haapala J. & Perovich D.K. 2010. Seasonality of spectral albedo and transmittance as observed in the Arctic Transpolar Drift in 2007. *Journal of Geophysical Research—Oceans 115*, C11011, doi: 10.1029/2009JC006074.

Nicolaus M., Hudson S.R., Gerland S. & Munderloh K. 2010. A modern concept for autonomous and continuous measurements of spectral albedo and transmittance of sea ice. *Cold Regions Science and Technology 62*, 14–28.

Pavelsky T.M. & Smith L.C. 2004. Spatial and temporal patterns in Arctic river ice breakup observed with MODIS and AVHRR time series. *Remote Sensing of Environment 93*, 328–338.

Pedersen C.A., Hall R., Gerland S., Sivertsen A.H., Svenøe T. & Haas C. 2009. Combined airborne profiling over Fram Strait sea ice: fractional sea-ice types, albedo and thickness measurements. *Cold Regions Science and Technology 55*, 23–32.

Perovich D.K. 1998. The optical properties of the sea ice. In M. Leppäranta (ed.): *Physics of ice-covered seas*. Pp. 195–230. Helsinki: University of Helsinki Press.

Perovich D.K. 2005. On the aggregate-scale partitioning of solar radiation in Arctic sea ice during the surface heat budget of the Arctic Ocean (SHEBA) field experiment. *Journal of Geophysical Research—Oceans 110*, C03002, doi: 10.1029/2004JC002512.

Perovich D.K., Cota G.F., Maykut G.A. & Grenfell T.C. 1993. Biooptical observations of first-year Arctic sea ice. *Geophysical Research Letters 20*, 1059–1062.

Perovich D.K. & Elder B. 2002. Estimates of ocean heat flux at SHEBA. *Geophysical Research Letters 29*, article no. 1344, doi: 10.1029/2001GL014171.

Perovich D.K., Grenfell T.C., Light B. & Hobbs P.V. 2002. Seasonal evolution of the albedo of multiyear Arctic sea ice. *Journal of Geophysical Research—Oceans 107*, article no. 8044, doi: 10.1029/2000JC000438.

Perovich D.K., Grenfell T.C., Richter-Menge J.A., Light B., Tucker W.B. III. & Eicken H. 2003. Thin and thinner: sea ice mass balance measurements during SHEBA. *Journal of Geophysical Research—Oceans 108*, article no. 8050, doi: 10.1029/2001JC001079.

Perovich D.K., Nghiem S.V., Markus T. & Schweiger A. 2007. Seasonal evolution and interannual variability of the local solar energy absorbed by the Arctic sea ice–ocean system. *Journal of Geophysical Research—Oceans 112*, C03005, doi: 10.1029/2006JC003558.

Richter-Menge J.A., Perovich D.K., Elder B.C., Claffey K., Rigor I. & Ortmeyer M. 2006. Ice mass-balance buoys: a tool for measuring and attributing changes in the thickness of the Arctic sea-ice cover. *Annals of Glaciology 44*, 205–210.

Shirasawa K., Ingram R.G. & Hudier E.J.J. 1997. Oceanic heat fluxes under thin sea ice in Saroma-ko Lagoon, Hokkaido, Japan. *Journal of Marine Systems 11*, 9–19.

Sturm M., Holmgren J. & Perovich D.K. 2002. Winter snow cover on the sea ice of the Arctic Ocean at the surface heat budget of the Arctic Ocean (SHEBA): temporal evolution and spatial variability. *Journal of Geophysical Research—Oceans 107*, article no. 8047, doi: 10.1029/2000JC000400.

Tschudi M.A., Maslanik J.A. & Perovich D.K. 2008. Derivation of melt pond coverage on Arctic sea ice using MODIS observations. *Remote Sensing of Environment 112*, 2605–2614.

Winther J.-G., Edvardsen K., Gerland S. & Hamre B. 2004. Surface reflectance of sea ice and under-ice irradiance in Kongsfjorden, Svalbard. *Polar Research 23*, 115–118.